



This is not the version of record. The full version of Plint, A. Guy, Uličný, David, Čech, Stanislav, Walaszczyk, Ireneusz, Gröcke, Darren R., Laurin, Jirí, Shank, Joel A. and Jarvis, Ian (2022) Trans-Atlantic correlation of Late Cretaceous high-frequency sea-level cycles. *Earth and Planetary Science Letters*, 578, p. 117323 can be found at <https://doi.org/10.1016/j.epsl.2021.117323>

1 **Trans-Atlantic correlation of Late Cretaceous high-frequency sea-level cycles**

2
3
4 A. Guy Plint^{a,b}, David Uličný^{c,d}, Stanislav Čech^e, Ireneusz Walaszczyk^f, Darren R.
5 Gröcke^g, Jiri Laurin^c, Joel A. Shank^{a,h}, Ian Jarvisⁱ

6
7 a. Department of Earth Sciences, the University of Western Ontario, London, Ontario,
8 N6A 5B7, Canada. gplint@uwo.ca

9 b. Corresponding author

10 c. Institute of Geophysics, Academy of Sciences of the Czech Republic, Boční II/1401,
11 141 31 Praha 4, Czech Republic.

12 d. Institute of Geology and Paleontology, Faculty of Science, Charles University,
13 Albertov 6, 128 43 Praha 2, Czech Republic

14 e. Czech Geological Survey, Klarov 3, 118 21 Praha 1, Czech Republic.

15 f. Faculty of Geology, University of Warsaw, Al. Żwirki i Wigury 93, PL-02-089
16 Warszawa, Poland,

17 g. Department of Earth Sciences, University of Durham, Durham, DH1 3LE, UK.

18 h. Present address: ExxonMobil Canada East, 100 New Gower St., St. John's,
19 Newfoundland, A1C 6K3, Canada.

20 i. Department of Geography, Geology and the Environment, Kingston University
21 London, Penrhyn Road, Kingston upon Thames, KT1 2EE, UK

22 **Keywords:** Upper Cretaceous, Eustasy, Bohemian Basin, Western Canada Foreland
23 Basin, Sea-Level Change.

24

25 **ABSTRACT**

26 Previous studies of Cretaceous sedimentary rocks have used multi-proxy correlation
27 methods to suggest eustatic change, modulated by the c. 400 kyr long eccentricity
28 rhythm. Although numerous authors have inferred eustatic changes on shorter
29 timescales, none have demonstrated synchronous sea-level changes in separate
30 basins on different plates, thousands of kilometres apart. Our study integrates basin-
31 scale, three-dimensional sequence architecture, molluscan biostratigraphy, and carbon-
32 isotope chemostratigraphy to demonstrate synchronous sea-level changes in upper
33 Turonian to lower Coniacian shallow-marine clastic successions in the Western Canada
34 Foreland Basin, and the Bohemian Cretaceous Basin. Depositional sequences in both
35 basins are plotted in a common time domain using an astronomically calibrated age
36 model, allowing direct comparison. In both basins, at least seven major transgressive
37 events can be shown to be synchronous within the limits of combined biostratigraphic
38 and chemostratigraphic resolution. 'Major' and 'minor' sequences of late Turonian age
39 appear to have been paced, respectively, by the long (c. 400 kyr) and short (c. 100 kyr)
40 eccentricity cycles. In contrast, early Coniacian sequences evidence pacing by the c.
41 38 kyr obliquity rhythm. Stratal architecture suggests that sequences developed in
42 response to eustatic changes of c. 14 – 20 m at average rates ranging 0.08 to > 1.3
43 m/kyr. At a time of 'warm greenhouse' climate, sea-level change of this magnitude and

44 timescale may not be explicable entirely as a result of thermal- and aquifer-eustasy, and
45 hence glacio-eustasy may also have been a contributing factor.

46

47 **1. Introduction**

48 Many Cretaceous shallow-marine clastic successions are characterized by
49 transgressive–regressive sequences in which facies changes are suggestive of relative
50 sea-level oscillations of < c. 30 m, commonly on a timescale of < c. 500 kyr. Although
51 the cyclicity has in cases been attributed to tectonic mechanisms (Kamola and Huntoon,
52 1995), there is increasing acceptance of the idea that many of these high-frequency
53 sequences are of eustatic origin, linked to Milankovitch-band climatic cycles (Gale et al.,
54 2002; Voigt et al., 2006; Laurin and Sageman, 2007; Plint and Kreitner, 2007; Uličný et
55 al., 2014; Lin et al., 2021). Definitive evidence of synchronous sea-level changes
56 between separate basins, especially at < 400 kyr timescale, is still rarely presented
57 (Wilmsen, 2007; Gale et al., 2008). Because of the inferred amplitude and frequency of
58 these sea-level changes, it has been postulated that they could only be attributed to
59 glacio-eustasy (e.g. Miller et al., 2005). This idea is supported by some climate model
60 results (Flögel et al., 2011), and by the presence of Early Cretaceous (Valanginian to
61 Aptian) glacial tills, ice-marginal deposits, and dropstones in the Eromanga Basin of
62 Australia, deposited at a palaeolatitude of between 70 and 80 °S (Alley et al. 2020).
63 The inference of Cretaceous glacio-eustasy is, however, highly controversial in view of
64 faunal, floral, sedimentary, and geochemical evidence that indicate that much of the
65 Cretaceous Period was a greenhouse world, apparently lacking polar ice caps. Recent
66 studies (Hay and Floegel, 2012; Kidder and Worsley, 2012; Sames et al., 2016, 2020;
67 Ray et al., 2019) now emphasize that the Cretaceous climate was not uniformly
68 equable, but oscillated between ‘cool’, ‘warm’ and ‘hot’ greenhouse phases. During

69 warm and hot greenhouse times, polar ice formation, and hence glacio-eustasy, was
70 considered improbable.

71 A solution to the mechanistic dilemma posed by high-frequency sequences was
72 the proposal of 'aquifer eustasy' (Hay and Leslie, 1990), by which cyclical climate
73 changes caused terrestrial aquifers to alternately fill and drain, resulting, respectively, in
74 sea-level fall, and rise. The amplitude and timescale of aquifer eustasy is, however,
75 subject to wide uncertainty. In their original proposal, Hay and Leslie (1990) estimated
76 that *complete* filling and emptying of terrestrial aquifers might, after isostatic
77 compensation, change sea-level by up to 50 m on a timescale of 10^4 to 10^5 years. In
78 an attempt to explain Milankovitch-band sea-level changes recorded in Triassic rocks,
79 Jacobs and Sahagian (1993) examined the regions of present Earth that were affected
80 by 20 kyr cycles of monsoonal precipitation; they calculated that aquifer-eustasy might
81 contribute from 4 to 8 m of sea-level change, and that similar fluctuations might have
82 driven Triassic sea-level cycles of c. 10 m.

83 More recently, a series of papers (Wagreich et al. 2014; Sames et al. 2016,
84 Wendler and Wendler, 2016; Wendler et al. 2016, Sames et al. 2020) have emphasized
85 the potential importance of aquifer-eustasy, suggesting that, during the Cretaceous
86 greenhouse (and especially the mid-Cretaceous warm- to hot greenhouse), spatio-
87 temporal shifts in arid and humid zones would have promoted alternate filling and
88 emptying of aquifers in continental interiors, potentially resulting in 50 to perhaps as
89 much as 80 m of eustatic change on a c. 400 kyr timescale, or longer. However, such

90 high-amplitude aquifer eustasy has been challenged by numerical modeling of spatio-
91 temporal variation in the distribution of arid and humid zones for the Valanginian,
92 Turonian, and Maastrichtian (Davies et al. 2020). Model results showed that aquifer-
93 eustasy during these Stages was likely to be in the range of decimetres, and even with
94 extreme forcing, did not exceed 5 m. In a comprehensive review of Phanerozoic
95 eustasy, Simmons et al. (2020) concluded that, for the Cretaceous, a combination of
96 thermo-eustasy and aquifer-eustasy might be able to explain short-term (1.2 Myr or
97 less), eustatic change of c. 10 m, whereas eustatic change in excess of c. 15 m would
98 be unachievable without a contribution from glacio-eustasy.

99 Any discussion of eustatic mechanisms must be underpinned by tightly
100 constrained stratigraphic evidence for synchronous sea-level changes in widely
101 separated locations, preferably on different plates (Ray et al., 2019). The basis of
102 precise correlation is high-resolution biostratigraphy, but the evidence for synchronous
103 events is strengthened if the stratigraphic architecture of each basin-fill can be
104 established in three dimensions, and if an independent means of correlation, such as
105 chemostratigraphy can be used to support biostratigraphy. Stable carbon-isotope
106 stratigraphy has proven to be an effective high-resolution correlation tool (Jarvis et al.,
107 2006, 2015, 2021; Wendler, 2013; Uličný et al., 2014), and integrated biostratigraphy
108 and carbon-isotope stratigraphy have been used to demonstrate trans-Atlantic
109 correlation of Cenomanian eustatic cycles interpreted to correspond to the 405 kyr long
110 eccentricity cycle (Gale et al., 2008). The new results presented here not only
111 demonstrate synchronous eustatic change on a timescale varying from c. 400 kyr to as

112 little as c. 30 kyr, but also address a stratigraphic interval that commonly is punctuated
113 by numerous hiatuses that can make accurate identification and correlation of sea-level
114 events extremely difficult.

115 We present the results of a multi-proxy study of shallow marine, siliciclastic strata
116 of late Turonian to early Coniacian age that were deposited about 7000 km apart (Fig.
117 1). The stratigraphic interval spanning the Turonian–Coniacian (T–C) boundary is well-
118 suited to an inter-basinal study of mid-Cretaceous sea-level change. An important sea-
119 level fall near the T–C boundary has been widely interpreted (Jarvis et al., 2006; Uličný
120 et al., 2014). However, detailed inter-basinal correlation of high-frequency (i.e. \ll 1 Myr
121 duration) depositional sequences that span the late Turonian to early Coniacian has, in
122 many cases, been prevented by hiatuses such as the Navigation Hardground suite in
123 the classical Chalk sections of the Anglo-Paris Basin, or by regional erosional surfaces
124 that typify many clastic and carbonate sections in other basins (Olszewska-Nejbert,
125 2004; Jarvis et al., 2006, 2021; Shank and Plint, 2013; Walaszczyk et al., 2014; Gale,
126 2019).

127 Although the Western Canada Foreland Basin (WCFB) and Bohemian
128 Cretaceous Basin (BCB) discussed here differ markedly in area (c. 360,000 vs. c.
129 30,000 km² respectively), and in tectonic style (flexural vs. transtensional, respectively),
130 their sedimentary successions preserve evidence of high-frequency depositional
131 cyclicity on a timescale of \ll 1 Myr. The question of a eustatic control on these
132 sequences is here addressed through detailed correlation, based on a combination of

133 three-dimensional stratigraphic analysis in both basins, molluscan biostratigraphy
134 utilizing species common to both North America and Europe, and organic carbon-
135 isotope stratigraphy. Relatively high biostratigraphic resolution is afforded in the latest
136 Turonian to early Coniacian by a number of closely spaced biostratigraphic markers in
137 both North America and Europe (10 markers in c. 1 Myr, Figs. 2, 3; Walaszczyk et al.,
138 2010, 2014). In addition, because CO₂ is cycled through the ocean–atmosphere
139 system on a timescale of the order of 10³ yr (Siegenthaler and Sarmiento, 1993),
140 carbon-isotope stratigraphy potentially affords a comparable, <10 kyr degree of
141 temporal resolution. In this study, the chronostratigraphic timescale that serves as the
142 basis for correlation is derived from the reference δ¹³C time series of the Bch-1 core
143 (BCB; Uličný et al., 2014). This dataset represents, to date, the highest temporal
144 resolution among published Upper Turonian–Coniacian δ¹³C curves.

145

146 **2. Materials and methods**

147 2.1 Correlation methods

148 Regional stratigraphy in both the WCFB and BCB was established through the
149 correlation of transgressive–regressive depositional sequences, bounded by marine
150 flooding surfaces, using grids of hundreds to thousands of wireline logs, supplemented
151 by core and outcrop data (Plint et al., 1986; Hart and Plint, 1993; Laurin and Uličný,
152 2004, Uličný et al., 2009, 2014; Shank, 2012; Shank and Plint, 2013). Macrofossils in
153 outcrop and core were integrated into the three-dimensional physical stratigraphic
154 framework, which included sections sampled for carbon isotope analysis (Walaszczyk et

155 al., 2014). In the BCB, this included a continuous core in the Bch-1 research well, used
156 as a new reference section for the middle to upper Turonian and for the T–C boundary
157 (Uličný et al., 2014). A time-domain portrayal of the carbon-isotope curve from Bch-1
158 (Fig. 2), spanning the upper Turonian to lower Coniacian interval, provides a common
159 chronostratigraphic framework for trans-Atlantic correlation, based on a new
160 astrochronological timescale (Laurin et al., 2014, 2015). Age estimates in Ma given in
161 the present paper are based on this model and include error margins as specified in
162 Jarvis et al. (2015). The most tightly constrained correlation between the two basins
163 has been established between the LO (Lowest Occurrence) of *Prionocyclus germari*
164 (Reuss) and the LO of *Cremnoceramus crassus crassus* (Petrascheck), spanning ~ 700
165 kyr (Laurin et al., 2014; Figs. 2, 3). In order to provide a broader chemostratigraphic
166 context for the high-resolution correlations across the T–C boundary, a correlation of
167 the entire Upper Turonian is here proposed.

168

169 2.2. Stratigraphic data: Cardium Formation, Western Canada Foreland Basin

170 The Cardium Formation is a clastic, shallow-marine to alluvial unit, up to ~150 m
171 thick, that was deposited on a broad, low-gradient, NE-facing ramp that spanned the
172 proximal (western) foredeep of the WCFB. Abundant, publicly-accessible wireline logs
173 and cores have provided the data for an allostratigraphic subdivision of the formation,
174 based primarily on the correlation of marine transgressive or flooding surfaces (Plint et
175 al., 1986). Such an approach has allowed the internal architecture of the formation to

176 be determined in detail, and on a basin scale (Fig. 4).

177 The Cardium Formation comprises a stack of regionally mappable, disconformity-
178 bounded, sandier-upward successions, interpreted to comprise transgressive, highstand
179 and falling-stage deposits. Lowstand deposits are bounded below by unconformable 'E'
180 surfaces and above by transgressive 'T' surfaces. Lowstand units are typically
181 conglomeratic, lenticular in dip view, and form metres-thick, strike-elongate bodies
182 isolated on the outer part of the ramp. To seaward and landward of the lowstand
183 deposits, the bounding 'E' and 'T' surfaces merge into composite disconformities,
184 labelled E1 through E7 (Plint et al., 1986; Plint, 1988; Hart and Plint, 1993; Shank and
185 Plint, 2013; Figs. 3, 4). Transgressive surfaces are mantled by cm- to dm-thick veneers
186 of extra-basinal pebbles that were reworked landward from lowstand shoreface
187 deposits. Collectively, each of the upward-shoaling successions, plus the overlying
188 conglomeratic cap, is interpreted as a depositional sequence that records a full cycle of
189 relative sea-level change. Nine principal sequences have now been mapped within the
190 formation in Alberta and British Columbia. The nine sequences are organized into three
191 major progradational packages, the lower between surfaces E1 and E4, the middle
192 between surfaces E4 and E5, and the upper between surfaces E5 and E7 (Shank and
193 Plint, 2013; Figs. 3, 4).

194 Sequence stacking in the Cardium Formation becomes increasingly
195 progradational between surfaces E1 and E5, accompanied by an increasingly tabular
196 stratal geometry, both features being interpreted to indicate a gradual decrease in
197 flexural subsidence rate (Shank, 2012; Shank and Plint, 2013). Two thin, latest

198 Turonian sequences between E5 and E5.5 are sheet-like, onlap landward onto E5 and
199 indicate the onset of sea-level rise but no increase in subsidence rate. Slow subsidence
200 prevailed in the earliest Coniacian, resulting in condensation or non-deposition between
201 E5.5 and E6. Foredeep subsidence accelerated markedly following E6 time, resulting in
202 a dramatic westward thickening of the interval between E6 and E7 (Shank and Plint,
203 2013; Figs. 3, 4).

204 A relatively expanded, shore-proximal section through the Cardium Formation,
205 fully exposed on the Bow River at Horseshoe Dam, Alberta (51° 07' 04.451" N 115° 02'
206 11.451" W; Fig. S1), was chosen for detailed sequence- and biostratigraphic study
207 (Shank and Plint, 2013; Walaszczyk et al., 2014; Fig. 3). The entire succession at
208 Horseshoe Dam was sampled at 0.5 m intervals for carbon isotopes, and a
209 supplementary section at Ghost River (51° 16' 15.391" N 114° 55' 09.231" W; Figs. 3,
210 S1), was also sampled, with sample spacing ranging from 1 m to as little as 0.2 m in the
211 vicinity of the Turonian–Coniacian boundary to better characterize the isotopic changes
212 across that interval. Additional data, in particular the LO of *C. deformis erectus*, and an
213 auxiliary C-isotope curve, based on samples with 0.5 m spacing, were obtained from a
214 distal basin succession at Deer Creek (Montana). Wireline logs allowed the Deer Creek
215 section to be correlated to Horseshoe Dam (Fig. S2; Shank and Plint, 2013; Walaszczyk
216 et al., 2014).

217

218 2.3. Stratigraphic data: Jizera and Teplice Formations, Bohemian Cretaceous Basin,

219 Czech Republic

220 In the BCB, the Cardium Formation has temporal equivalents in the Jizera and
221 Teplice formations (Čech and Uličný, 2021, and references therein). These clastic units
222 were deposited in nearshore deltaic, shoreface, and offshore to hemipelagic
223 environments in several fault-bounded sub-basins within a major, reactivated intra-
224 continental fault zone (Voigt et al., 2008). The correlations presented here focus on the
225 northwestern sub-basin of the BCB where the genetic sequence stratigraphy and
226 detailed biostratigraphy of the sandstone-dominated deltaic wedges are best
227 documented (Uličný et al., 2009). The Český Ráj depocentre is of particular importance
228 because the T–C boundary is preserved there in a well-exposed succession of coarse-
229 grained deltas (Čech and Uličný, 2021).

230 The Jizera Formation (Figs. 3, 5) in the central BCB region is dominated by
231 strongly bioturbated, mixed siltstones and marlstones that indicate deposition in
232 offshore to hemipelagic environments that grade landward into distal prodelta to lower
233 shoreface environments. Relative to the location of the Bch-1 core hole, the nearest
234 shoreline lay about 35 km to the NW (Uličný et al., 2014). In the regional genetic-
235 stratigraphic scheme based on maximum transgressive surfaces (Uličný et al., 2009),
236 the Jizera Formation of the Český Ráj depocentre comprises genetic sequences TUR 5
237 through 6/1 (Fig. 5), with the base of TUR 6/1 much less pronounced than in the type
238 area of the western BCB (Laurin and Uličný, 2004). This part of the study interval was
239 generally characterized by relatively high sedimentation rates (c. 20 cm/kyr) in a
240 hemipelagic realm and preserves a conspicuous cyclic signal in elemental proxy

241 parameters such as the Si/Al ratio (Fig. 3). Fluctuations in this ratio are interpreted as a
242 record of precession cycles modulated by short eccentricity, that governed the input of
243 coarser grained clastics into the basin (Fig. S4; Chroustová et al., 2021).

244 The highest upper Turonian and lower Coniacian strata in the Český Ráj
245 depocentre comprise sandstone-dominated, Gilbert-type deltas that prograded
246 generally southward from the faulted basin margin, into water as much as c. 100 m
247 deep. The deltaic clinothems pass downdip into heterolithic, turbidite-dominated
248 bottomset facies, and further basinward into offshore mudstone and marlstone of the
249 Teplice Formation (Laurin and Uličný, 2004; Uličný et al., 2009, 2014; Čech and Uličný,
250 2021). A number of deltaic sandstone wedges are grouped into a single package, the
251 Hrubá Skála Sandstone Member of the Teplice Formation, that shows a forestepping
252 geometry of thick, deep-water delta bodies in the lower part, overlain by a much thinner
253 package of backstepping shallow-water delta bodies, in turn capped by offshore marly
254 mudstone (Fig. 5). The Hrubá Skála Sandstone and its distal correlatives correspond to
255 sequences TUR 7 and CON 1 defined in the western part of the basin (Uličný et al.,
256 2009). Within the Hrubá Skála Sandstone, individual prograding deltaic clinothems,
257 separated by minor transgressive surfaces, were labelled HS-1 through HS-8 by Čech
258 and Uličný (2021). The shift from a long-term progradational to a retrogradational
259 stacking pattern occurs between HS-6 and HS-7 (Fig. 5).

260 Genetic sequences TUR 5 and TUR 6/1 in the BCB form a long-term
261 progradational succession that overlies a major, basinwide transgressive surface and is

262 terminated above by a flooding surface that marks the lowest occurrence of the
263 ammonite *Prionocyclus germari*. Sequence TUR 6/2 contains the first steeply-dipping,
264 sand-dominated clinothems belonging to the Hrubá Skála Sandstone, but as a whole
265 TUR 6/2 shows a relative backstep and is separated from the younger TUR 7 sequence
266 by another major transgressive surface. The subsequent long-term progradation of
267 deltaic units HS-2 to HS-6 is interrupted by a transgressive event at the LO of
268 *Cremnoceramus waltersdorfensis waltersdorfensis* (Andert). The change from
269 progradation to retrogradation at the base of local sequence HS-7 coincides with the LO
270 of *Cremnoceramus crassus inconstans* (Woods). The final drowning of the entire Hrubá
271 Skála deltaic system coincides with the base of the *C. crassus crassus* Zone (base of
272 CON 2 sequence; Čech and Uličný, 2021). Despite the tectonic activity at the adjacent
273 basin margin and differential subsidence in the depocentre (Fig. 5), the above
274 transgressive surfaces are correlated widely, interpreted as basinwide and most likely of
275 eustatic origin.

276 Three significant regressive intervals, attributed to relative sea-level falls, stand
277 out in the BCB: (1) the terminal lowstand of sequence TUR 5; (2) long-distance
278 progradation of HS-2 (= TUR 7 elsewhere in the basin); (3) marked progradation of
279 small-scale sequences HS-4 and HS-5 associated with offlap within the CON 1
280 sequence (Čech and Uličný, 2021).

281

282 2.4. Analytical methods.

283 The carbon-isotope data presented here (Figs. 2, 3) are based on: (i) previously

284 published datasets of $\delta^{13}\text{C}_{\text{org}}$ and $\delta^{13}\text{C}_{\text{carb}}$ from the Bch-1 core in the BCB (Uličný et al.,
285 2014; Jarvis et al., 2015); (ii) a new suite of $\delta^{13}\text{C}_{\text{org}}$ analyses of samples from Alberta
286 and Montana. Analytical work was undertaken at the Stable Isotope Biogeochemistry
287 Laboratory (SIBL) at the University of Durham. Sedimentary samples were ground to a
288 fine powder (ca. 10 μm) using a Retsch agate mortar grinder RM100. The bulk rock
289 powders (ca. 5 mL) were decalcified using 3 M HCl overnight at room temperature (20
290 $^{\circ}\text{C}$) in 50 mL centrifuge tubes. Insoluble residues were rinsed three to four times with
291 deionized water, subsequently dried at 50 $^{\circ}\text{C}$, reground in an agate mortar, and stored
292 in glass vials until isotopic analysis could be performed.

293 Organic carbon isotope ($\delta^{13}\text{C}_{\text{org}}$) measurements were performed on 2.5–3 mg
294 splits of the insoluble residues using a Costech elemental analyser (ESC 4010)
295 connected to a Thermo Scientific Delta V Advantage isotope ratio mass spectrometer
296 via a ConFlo III interface. Carbon isotope ratios are reported in standard delta (δ)
297 notation in per mil (‰) relative to VPDB. Data accuracy was monitored through
298 analyses of international and in-house standards calibrated against the international
299 standards (viz., IAEA-CH-3, IAEA-CH-6, IAEA-CH-7, IAEA-N-1, IAEA-N-2, NBS 24,
300 USGS40). Analytical uncertainty for carbon isotope measurements was $\pm 0.1\text{‰}$ for
301 replicate analyses of standards and $< 0.2\text{‰}$ on replicate sample analyses.

302

303 2.5 Assessment of subsidence and sea-level change

304 In the Cardium Formation, the E3 to E7 interval provides the best opportunity to

305 estimate the magnitude of eustatic change, based on stratal offlap and onlap patterns,
306 and from a determination of the pattern of subsidence. Shank (2012) showed, on the
307 basis of isopach mapping, that regional flexural tectonic subsidence rate decelerated
308 from E1 to E3, became low to negligible between E3 and E6, but then accelerated
309 markedly between E6 and E7. For the E3 to E6 interval, isopach maps showed that
310 subsidence was primarily due to the isostatic effect of a 'slab load' of sediment and
311 water. In order to make simple estimates of subsidence based on isopach maps, Airy
312 isostasy was assumed; shallowly buried, semi-compacted sediment density was
313 assumed to be 2.3 g/cm^3 , asthenospheric mantle = 3.4 g/cm^3 and water = 1 g/cm^3 . The
314 observed thickness of mixed mudstone-sandstone lithologies was decompacted to a
315 nominal 'shallow burial depth' by expansion by 30%. Supplementary Data provides
316 more detailed discussion of estimates of sea-level change in the Cardium Formation.

317 For the BCB, estimated subsidence rates during the Turonian and Coniacian
318 were published by Uličný et al. (2009) and the reader is referred to the Appendix in that
319 paper for the decompaction procedure applied.

320

321 **3. Results**

322 3.1 Inter-basinal correlation

323 The Canadian and Bohemian basins were characterized by temporally and
324 spatially non-uniform rates of subsidence that complicate comparison of sequence
325 stacking patterns. In the WCFB, the nearshore succession close to the T–C boundary
326 is punctuated by hiatuses, whereas in the BCB the stage boundary interval is recorded

327 in both nearshore and offshore facies (Figs. 2–5). Correlations can nevertheless be
328 established because of the availability of high-resolution biostratigraphic and carbon-
329 isotope data, coupled with the chronostratigraphic age model, that allow the succession
330 of depositional sequences to be compared between basins (Laurin et al., 2014, 2015;
331 Fig. 2). Importantly, the successions of inoceramid bivalves in the Canadian and
332 Bohemian basins are essentially identical (Walaszcyk et al., 2014; Čech and Uličný,
333 2021), and the lowest occurrences of key taxa appear to be synchronous within the
334 resolution of the $\delta^{13}\text{C}$ chronostratigraphy.

335 The most marked difference between the two datasets is in the long-term
336 sequence stacking patterns. In particular, the timing of maximum offlap in the T–C
337 interval differs significantly between the WCFB and BCB. The interval represented by
338 the E5 surface in the WCFB occurs in the latest Turonian and appears to span 89.9 –
339 90.1 Ma (Fig. 6). In the BCB, the main hiatus is in the early Coniacian, with maximum
340 offlap at c. 89.6 Ma (Fig. 6). This discrepancy is the result of differences in the timing of
341 tectonic events – temporary cessation of flexural subsidence in the WCFB vs.
342 accelerated subsidence in the north-eastern BCB (Shank and Plint, 2013; Čech and
343 Uličný, 2021). In datasets of lower stratigraphic resolution, these two unconformities
344 could easily be misinterpreted as the same “eustatic” event.

345 Viewed at a higher stratigraphic resolution, four major transgressive events
346 coincide, respectively, with the LOs of *P. germari*, *C. waltersdorfensis waltersdorfensis*,
347 *C. crassus inconstans* and *C. crassus crassus*. The LO of *C. w. waltersdorfensis* was

348 not identified at Horseshoe Dam, but can be correlated from other sections to a level
349 immediately above the T5.5 surface (Walaszczyk et al., 2014). This correlation is
350 further supported by the marked minimum in $\delta^{13}\text{C}_{\text{org}}$ in the Ghost River section,
351 interpreted as a record of part of the Navigation carbon-isotope event (CIE) (Fig. 3). In
352 addition to the above four flooding surfaces, three other surfaces are less well
353 constrained biostratigraphically, but are correlated on the basis of $\delta^{13}\text{C}$ trends: (1) the
354 basinwide flooding at base of the TUR 5 sequence in the BCB appears to correlate to
355 the E1a surface in the WCFB; (2) an unnamed but marked transgressive surface early
356 in TUR 5, at the level of the Bridgewick CIE in the BCB, correlates to the E2 surface in
357 the WCSB; and (3) the flooding surface at the base of TUR 6/1 (Laurin & Uličný, 2004)
358 overlies a short-term lowstand recognized elsewhere in Central Europe (Čech and
359 Uličný, 2021), and matches a similarly pronounced $\delta^{13}\text{C}$ trend across the E4 surface in
360 the WCFB (Fig. 3).

361 Whereas the LO of *P. germari* is associated with marked flooding events in both
362 regions, the subsequent transgression associated with the *Didymotis* Event “0” in the
363 BCB and the base of TUR 7 sequence, is not recognizable at Horseshoe Dam: either a
364 coeval transgressive event did not occur there or, more probably, equivalent strata
365 below the E5 surface are only preserved in the distal, subsurface part of the basin (Figs.
366 3, 6).

367 In addition to the foregoing seven transgressive events, here considered
368 synchronous within the resolution of the bio- and $\delta^{13}\text{C}$ stratigraphy, prominent lowstand
369 events also correlate between the BCB and WCFB. At least three high-frequency

370 pulses of sea-level rise followed the E4 lowstand in the WCFB (Pattison and Walker,
371 1992), and these events are correlated to the TUR 5 lowstand–transgressive interval in
372 the BCB, spanning 4–5 precession cycles (Figs. 2, 6). The prominent offlapping to
373 lowstand package (Keith, 1991; Fraser, 2012; Fic, 2013) between surfaces E4 and E5
374 in the WCFB (Fig. 4) is correlative with the long-distance regression recorded by the
375 TUR 7 sequence in the BCB (Fig. 5; Uličný et al., 2009; Nádaskay and Uličný, 2014). A
376 falling stage to lowstand phase is interpreted in the BCB to represent local sequences
377 HS-4 through HS-6 in the *C.w. hannovrensis* Zone of the Hrubá Skála Sandstone (Čech
378 and Uličný, 2021) and may correlate to the E5.7 and E6 surfaces.

379

380 **4. Sea-level changes**

381 4.1. Timescale of sea-level change

382 A tentative, qualitative sea-level curve (Fig. 6) is based on the correlation of
383 principal transgressive and regressive events between the two study areas.
384 Comparison of the relative sea level histories to the Bch-1 age model reveals an
385 apparent change in the timing of the main transgressive and regressive events within
386 the studied interval. This change involves sea-level cycles, on at least two timescales,
387 both operating over < 1 Myr. Genetic sequences TUR 5 and 6/1 together represent c.
388 864 kyr in the Bch-1 age model, and sequence TUR 6/2 represents c. 382 kyr. The
389 duration estimates and patterns of cyclicity suggest control by the c. 400-kyr eccentricity
390 modulation of the precession rhythm. This is supported by the spectral estimate for the

391 Si/Al siliciclastic proxy that follows the transgressive–regressive pattern of genetic
392 sequences TUR5 through TUR7 and suggests an elevated power in the 400-kyr band
393 (Fig. S4).

394 In younger strata, the relative sea-level cycles appear to be of higher frequency.
395 Within TUR 7 sequence lasting c. 246 kyr, four short-term genetic sequences are
396 recognized (Čech and Uličný, 2021), giving an estimated duration of a short-term
397 sequence of c. 61 kyr. In the CON 1 sequence that lasted c. 243 kyr, six short-term
398 regressive pulses recognized by Čech and Uličný (2021) in HS 3-8 have, on average, a
399 duration of 40.5 kyr, whereas the correlative interval in the WCFB, between surfaces
400 E5.5 and E7, contains four principal sequences with an average duration of 67.5 kyr.
401 Both estimates are well below the 100 kyr eccentricity cycle; at least in the BCB, the
402 short-term cyclicity estimate is closest to the axial obliquity cycle (c. 38 kyr in the
403 Cretaceous; Laskar et al., 2004).

404 Simplistic estimates such as these need to be treated with caution, however. In
405 the BCB, the total number of local sequences is based on an incompletely preserved
406 record of the Hrubá Skála deltaic complex. Potential additional, unrecorded sequences
407 would further shorten the estimated cycle duration; at the same time, some sequences
408 may have recorded episodes of delta lobe switching, superimposed on longer-term
409 relative sea-level trends. The correlation of high-frequency sequences appears to be
410 closest in the *C. c. inconstans* Zone that lasted about 60 kyr (Laurin et al., 2014): in both
411 basins, this Zone contains two principal accommodation cycles (Fig. 3). The potential
412 relationship of these sea-level cycles to either precessional or obliquity forcing is

413 unclear.

414

415 4.2. Amplitude and rate of sea-level change

416 The amplitude of eustatic change in both the WCSB and BCB has been
417 estimated on the basis of mapped regional stratal geometry and thickness, calibrated
418 against absolute age derived from isotopic data and an age model (Fig. 6). These data
419 allow net subsidence rate to be estimated for each stratal package. An appreciation of
420 subsidence rate is a prerequisite to any attempt to determine eustatic change. Details
421 of the method by which eustatic change was estimated are given in Supplementary
422 Data.

423 In the WCFB, eustatic fall below E4 (Fig. 6) and subsequent transgression above
424 E4 is estimated to have been about 14 m, with an average rate of change estimated at
425 c. 0.28 m/kyr. The E4.5 to E5 interval was a time of negligible flexural subsidence. It is
426 characterized by the offlap of at least 20 small sequences below E5, which is then
427 overlain by two overlapping wedges comprising the E5 to E5.2 and E5.2 to E5.5
428 sequences. The observed offlap and onlap geometries below and above E5 indicate
429 net eustatic fall and subsequent rise of c. 20 m, implying an average rate of eustatic
430 change of c. 0.08 m/kyr for each half cycle. The E5.5 to E6 package also records
431 negligible flexural subsidence, and facies offset across E5.5 suggests eustatic rise of at
432 least 15 m, with comparable fall across E6, at a rate of c. 0.2 m/kyr. The E6 to E7
433 interval was characterized by renewed rapid flexural subsidence, at about 1.3 m/kyr,

434 and comprises two sequences, each spanning ~ 30 kyr. Relative sea-level fall events at
435 E6.5 and E7 imply that the rate of eustatic fall must have twice exceeded c. 1.3 m/kyr.

436 In the BCB, eustatic fall is inferred to have matched or exceeded subsidence rate
437 during TUR 7 regression (equivalent to E5 to E5.5 package), at an average rate of c.
438 0.2 – 0.3 m/kyr (Uličný et al., 2009). The relative sea-level rise that drowned the TUR 7
439 package (HS-2) in the latest Turonian involved at least 13 m of eustatic component
440 (comparable to 15 m at equivalent E5.5 surface in Alberta) at a rate of c. 0.5 m/kyr.
441 Thus, evidence from both study areas suggests that Late Turonian sea-level fell in the
442 range of 14 – 20 m at rates of 0.08 to 0.28 m/kyr, whereas in the Early Coniacian, the
443 frequency of eustatic change appears to have been higher, involving excursions of 15 m
444 or more, at rates in the range 0.5 to 1.3 m/kyr.

445

446 **5. Discussion**

447 Although synchronous short-term sea-level changes on a timescale of as little as
448 30 kyr are indicated by our data, their causal mechanisms remain difficult to determine.
449 It is widely acknowledged that short-term (< 1 Myr) Cretaceous eustatic changes are
450 controlled by orbitally driven climate cycles that can change sea-level through three
451 mechanisms: (1) the upper limits of thermal-eustasy (maximum of 10 m) and (2) glacio-
452 eustasy (c. 200 m) are well-known, whereas estimates of (3) aquifer-eustasy are very
453 variable, ranging from 4 to 100 m (Ray et al., 2019).

454 The relative importance of glacio- and aquifer-eustasy is considered to vary
455 between cool, warm and hot greenhouse climate phases. Some have argued that the

456 Turonian was an ice-free 'warm greenhouse' where only thermal- and aquifer-eustasy
457 were responsible for short-term eustatic change (Ladant and Donnadieu, 2016; O'Brien
458 et al., 2017; Sames et al., 2016, 2020). Aquifer-eustasy is driven by expanding and
459 contracting humid and arid climate zones. Arid regions have the greatest potential to
460 store and release groundwater because aquifers in humid regions are always nearly full.
461 This mechanism has been estimated to operate on a timescale of 10^4 to 10^5 years, and
462 to yield c. 10 – 50 m of eustatic change (Hay and Leslie, 1990; Sames et al., 2016).
463 This conclusion was challenged by Davies et al. (2020) who modeled the climatic
464 forcing effect of varying atmospheric CO₂ on the areal extent of arid zones. Their study
465 suggested that aquifer-eustasy in the Turonian would be < 2 m.

466 Ray et al. (2019) pointed out that increased global temperature should, according
467 to the aquifer-eustasy concept of Wendler and Wendler (2016), produce the highest
468 humidity and most effective groundwater recharge, and consequently the largest
469 eustatic response. Broad-based estimates of eustatic change through the Cretaceous
470 showed, however, that the peak greenhouse (Albian to Coniacian) was also
471 characterized by the lowest amplitude of eustatic change (c. 30 m). This reasoning led
472 Ray et al. (2019) to conclude that glacio-eustasy must have played some part in
473 controlling sea-level, even at peak greenhouse.

474 As shown in Figure 6, the most prominent transgressive events in the study
475 interval coincide with marked negative $\delta^{13}\text{C}$ intervals (the Bridgewick and Navigation
476 CIEs; $\delta^{13}\text{C}$ trough on top of the Hitch Wood 2 CIE). This observation may provide

477 support for an aquifer-eustatic mechanism which, as shown by Laurin et al. (2019),
478 could have resulted in coupling between the global hydrological and carbon cycles.
479 Storage of organic matter on land in lakes and environments of high water-table would
480 coincide with charged aquifers and lower sea levels and increased $\delta^{13}\text{C}$ values – and
481 vice versa. The covariance between the inferred sea level curve and $\delta^{13}\text{C}$ values (Fig.
482 6) is, however, far from universal.

483 The Cardium Formation may provide evidence for co-variance between sea-level
484 and hydrological changes over the Rocky Mountain Cordillera. Extra-basinal
485 conglomerate is present mainly in lowstand shoreface deposits, whereas highstand and
486 falling-stage deposits are dominated by sandstone. This observation may provide
487 independent evidence for a linkage between sea-level fall and higher river discharge
488 that triggered a short-lived advance of the gravel front in rivers, allowing pebbles to
489 reach the lowstand shoreline. Eustatic fall of the estimated c.10 – 20 m would, alone,
490 be inadequate to steepen river gradients across a coastal plain at least 100 km wide,
491 sufficient to initiate gravel supply to the coast (Plint et al., 2018).

492 Although there appears to be an increase in the frequency of short-term sea-level
493 cycles near the T–C boundary, from eccentricity-dominated to obliquity-dominated, this
494 inference requires further testing with expanded data sets having improved stratigraphic
495 resolution. Our observations, nonetheless, suggest that the interpreted rates and
496 amplitudes of late Turonian and early Coniacian eustatic change, and associated pulses
497 of molluscan evolution, could have been superimposed on either a secular trend, or a
498 singular change in the climate system that led to a shift towards higher-frequency and

499 higher-rate sea-level changes in the Coniacian. The evidence for c. 14 – 20 m of short-
500 term eustatic change, at rates ranging from 0.08 to 1.3 m/kyr, may imply control by a
501 combination of aquifer- and glacio-eustasy, supplemented by a minor thermo-eustatic
502 component (cf. Simmons et al. 2020). Our estimates of eustatic change are smaller
503 than the c. 50 m maximum range inferred on the basis of the stratal stacking pattern in
504 Middle Turonian to Lower Coniacian strata in New Mexico (Lin et al., 2021). Although
505 the $\ll 1$ Myr timescale of change in both studies is comparable, direct correlation of
506 results is precluded by the lack of a carbon-isotope or biostratigraphic framework in the
507 study of Lin et al. (2021).

508

509 **6. Conclusions**

- 510 1. In upper Turonian to lower Coniacian strata, at least seven major transgressive
511 events documented in the WCFB and the BCB are shown to be synchronous within the
512 limits of biostratigraphic and stable C-isotope resolution, implying a eustatic control.
513 Eustatic changes are estimated to have been in the range 14 – 20 m, and possibly
514 more. Inferred average rates of sea-level change range from 0.08 to > 1.3 m/kyr.
- 515 2. The timing of major flooding and lowstand events, based on the available age model,
516 suggests that sea-level changes during the late Turonian took place on a timescale
517 close to the 400- and 100-kyr eccentricity cycles. In contrast, early Coniacian
518 sequences in the BCB, and, in part, those in the WCFB, appear to have been paced by
519 the obliquity rhythm.

520 3. The succession of high-frequency sea-level changes identified here explains why the
521 T–C boundary interval, worldwide, is marked by one or more hiatuses. The exact timing
522 of major offlap episodes, however, depended on tectonic processes in individual basins,
523 and the amalgamation of several short-term hiatuses, and/or poor stratigraphic
524 resolution could lead to incorrect age assignment of unconformities and of sea-level
525 histories.

526 4. It is not possible to provide definitive evidence for or against a glacio-eustatic
527 mechanism acting in this time interval. Glacio-eustasy, driven by Milankovitch-band
528 climatic cycles, is proven to provide the necessary amplitude and frequency necessary
529 to explain our observations. If the conclusions of Simmons et al. (2020) are accepted,
530 then our interpreted eustatic changes of 14 to 20 m suggest some component of glacio-
531 eustasy. Although the timescale and potential amplitude of aquifer-eustasy is less well-
532 understood, it is nevertheless also a plausible contributor to Cretaceous eustatic
533 change, and the correlation of major flooding events to lowered $\delta^{13}\text{C}$ values supports
534 the operation of this mechanism in at least part of the record.

535

536 **Acknowledgements**

537 AGP acknowledges funding, spanning several grant cycles, of his research on Western
538 Canada Cretaceous stratigraphy, by the Natural Sciences and Engineering Research
539 Council of Canada (NSERC). He thanks Neil Landman for identifying *Scaphites patulus*
540 from Horseshoe Dam. We thank S. Galić, M. Grifi, R. Langham and T. Plint for their
541 assistance in the field. DU, SČ and JL were supported by the Czech Science

542 Foundation (GAČR), grant No. 17-10982S, and by the Czech Academy of Sciences
543 through Programme 67985530. SČ acknowledges long-term support by the Czech
544 Geological Survey. Field and laboratory assistance by M. Vopat and A. Uličný is
545 appreciated. DG and IJ were funded by UK Natural Environment Research Council
546 (NERC) grants NE/H021868/1 and NE/H020756/1. IW was supported by the Polish
547 National Science Centre (NCN) Grant no. 2018/31/B/ST10/01820. JAS
548 acknowledges an NSERC postgraduate scholarship. We thank two anonymous
549 referees for their reviews of the manuscript.

550

551 **Author contributions**

552 The initial concept of the paper was developed jointly by AGP and DU in 2004, and
553 subsequently elaborated with input from DG and IJ in 2010. In Canada, AGP and JAS
554 undertook stratigraphic analysis and isotopic sampling, and IW conducted
555 biostratigraphic analysis. In the Czech Republic, DU and SČ undertook stratigraphic
556 analysis and isotopic sampling, SČ conducted biostratigraphic analysis, and JL
557 constructed the age model and evaluated astronomical signatures in elemental proxy
558 data. DG conducted carbon-isotope analyses on the WCFB samples. All authors
559 contributed to interpretation of data.

560

561 **Competing financial interests**

562 The authors declare no competing financial interests.

563

564 **References**

565 Alley, N.F., Hore, S.B., Frakes, L.A., 2020. Glaciations at high-latitude Southern

566 Australia during the Early Cretaceous. *Australian J. Earth Sci.* 67, 1045–1095.

567 Čech, S., Uličný, D., 2021. The Turonian–Coniacian stage boundary in an expanded

568 siliciclastic succession: integrated stratigraphy in deltaic through offshore facies,

569 Bohemian Cretaceous Basin. *Cret. Res.* 117, 104576

570 <https://doi.org/10.1016/j.cretres.2020.104576>.

571 Chroustová, M., Holcová, K., Laurin, J., Uličný, D., Hradecká, L., Hrnková, M., Čech, S.,

572 Hrouda, F., Jarvis, I., 2021 Response of foraminiferal assemblages to precession-

573 paced environmental variation in a mid-latitude seaway: Late Turonian greenhouse

574 of Central Europe. *Marine Micropal.* 167, 102025

575 <https://doi.org/10.1016/j.marmicro.2021.102025>.

576 Davies, A., Gréselle, B., Hunter, S.J., Baines, G., Robson, C., Haywood, A.M., Ray,

577 D.C., Simmons, M.D., van Buchem, F.S.P., 2020. Assessing the impact of aquifer-

578 eustasy on short-term Cretaceous sea-level. *Cret. Res.* 112, 104445

579 <https://doi.org/10.1016/j.cretres.2020.104445>.

580 Fic, J.D., 2013. Characterization of the lower shoreface to offshore reservoir facies of

581 the Cardium Formation in East Pembina, Alberta. M.Sc. thesis, University of

582 Calgary, 128 p.

583 Flögel, S., Wallmann, K., Kuhnt, W., 2011. Cool episodes in the Cretaceous – Exploring

584 the effects of physical forcings on Antarctic snow accumulation. *Earth Planet. Sci.*

585 Lett. 307, 279–288.

586 Fraser, J.A., 2012. High resolution sequence stratigraphy and reservoir characterization
587 of shoreline deposits of the Cardium Formation at West Pembina, Alberta. M.Sc.
588 thesis, University of Calgary, 89 p.

589 Gale, A., 2019. Correlation, age and significance of Turonian Chalk hardgrounds in
590 southern England and northern France: The roles of tectonics, eustasy, erosion
591 and condensation. *Cret. Res.* 103, 104164
592 <https://doi.org/10.1016/j.cretres.2019.06.010>.

593 Gale, A.S., Hardenbol, J., Hathway, B., Kennedy, W.J., Young, J.R., Phansalkar, V.,
594 2002. Global correlation of Cenomanian (Upper Cretaceous) sequences: Evidence
595 for Milankovitch control on sea level. *Geology* 30, 291–294.

596 Gale, A.S., Voigt, S. Sageman, B.B., Kennedy, W.J., 2008. Eustatic sea-level record for
597 the Cenomanian (Late Cretaceous) – Extension to the Western Interior Basin,
598 USA. *Geology* 36, 859–862.

599 Hart, B.S. Plint, A.G., 1993. Origin of an erosion surface in shoreface sandstones of the
600 Kakwa Member (Upper Cretaceous Cardium Formation, Alberta): Importance for
601 reconstruction of stratal geometry and depositional history. In: Posamentier, H.W.,
602 Summerhayes, C.P., Haq, B.U., Allen, G.P. (Eds.), *Sequence Stratigraphy and*
603 *Facies Associations*. Int. Assoc. Sedimentol. Spec. Pub. 18, Blackwell Science,
604 Oxford, 451–467.

605 Hay, W.W., Leslie, M.A., 1990. Could possible changes in global ground water reservoir

606 cause eustatic sea-level fluctuations? In: Revelle, R. (Ed.), *Sea Level Change*.
607 Nat. Res. Council, Studies in Geophys. Washington D.C. Nat. Acad. Press, 161–
608 170.

609 Hay, W.W., Flögel, S., 2012. New thoughts about Cretaceous climate and oceans.
610 *Earth-Sci. Rev.* 115, 262–272.

611 Jacobs, D.K., Sahagian, D.L., 1993. Climate-induced fluctuations in sea level during
612 non-glacial times. *Nature* 361, 710–712.

613 Jarvis, I., Gale, A.S., Jenkyns, H.C., Pearce, M.A., 2006. Secular variation in Late
614 Cretaceous carbon isotopes: a new $\delta^{13}\text{C}$ carbonate reference curve for the
615 Cenomanian–Campanian (99.6–70.6 Ma). *Geol. Mag.* 143, 561–608.

616 Jarvis, I., Trabucho-Alexandre, J., Gröcke, D.R., Uličný, D., Laurin, J., 2015.
617 Intercontinental correlation of organic carbon and carbonate stable isotope
618 records: evidence of climate and sea-level change during the Turonian
619 (Cretaceous). *Dep. Record* 1, 53–90.

620 Jarvis, I., Pearce, M., Püttmann, T., Voigt, S., Walaszczyk, I., 2021. Palynology and
621 calcareous nannofossil biostratigraphy of the Turonian – Coniacian boundary: the
622 proposed boundary stratotype at Salzgitter-Salder, Germany and its correlation in
623 NW Europe. *Cret. Res.* 123, 104782 <https://doi.org/10.1016/j.cretres.2021.104782>

624 Joo, Y.J., Sageman, B.S., 2014. Cenomanian to Campanian isotope chemostratigraphy
625 from the Western Interior Basin, U.S.A. *J. Sedim. Res.* 84, 529–542.

626 Kamola, D.L., Huntoon, J.E., 1995. Repetitive stratal patterns in a foreland basin
627 sandstone and their possible tectonic significance. *Geology* 23, 177–180.

- 628 Keith, D.A.W., 1991. Truncated prograding strandplain or offshore sand body? –
629 sedimentology and geometry of the Cardium (Turonian) sandstone and
630 conglomerate at Willesden Green field, Alberta. In: Swift, D.J.P., Oertel, G.F.,
631 Tillman, R.W., Thorne, J.A., (Eds.), Shelf sand and sandstone bodies, geometry,
632 facies and sequence stratigraphy. Int. Assoc. Sedimentol. Spec. Pub. 14,
633 Blackwell Science, Oxford, 457–487.
- 634 Kidder, D.L., Worsley, T.R., 2012. A human-induced hothouse climate? GSA Today 22,
635 4–11.
- 636 Ladant, J.-B., Donnadieu, Y., 2016. Palaeogeographic regulation of glacial events
637 during the Cretaceous supergreenhouse. Nature Comm. 7,
638 12771 <https://doi.org/10.1038/ncomms12771>.
- 639 Laskar, J., Robutel, P., Joutel, F., Gastineau, M., Correia, A.C.M., Levrard, B., 2004. A
640 long-term numerical solution for the insolation quantities of the Earth. Astron.
641 Astrophys. 428, 261–285 <https://doi.org/10.1051/0004-6361:20041335>.
- 642 Laurin, J., Uličný, D., 2004. Controls on a shallow-water hemipelagic carbonate system
643 adjacent to a siliciclastic margin: Example from Late Turonian of central Europe. J.
644 Sedim. Res. 74, 697–717.
- 645 Laurin, J., Sageman, B.B., 2007. Cenomanian–Turonian coastal record in SW Utah,
646 U.S.A.: Orbital-scale transgressive-regressive events during oceanic anoxic event
647 II. J. Sedim. Res. 77, 731–756.
- 648 Laurin, J., Čech, S., Uličný, D., Štaffen, Z., Svobodová, M., 2014. Astrochronology of

649 the Late Turonian: implications for the behavior of the carbon cycle at the demise
650 of peak greenhouse. *Earth Planet. Sci. Lett.* 394, 254–269.

651 Laurin, J., Meyers, S.R., Uličný, D., Jarvis, I., Sageman, B.B., 2015. Axial obliquity
652 control on the greenhouse carbon budget through middle- to high-latitude
653 reservoirs. *Paleoceanography* 30, 133–149.

654 Laurin, J., Barclay, R.S., Sageman, B.B., Dawson, R.R., Pagani, M., Schmitz, M.,
655 Eaton, J., McInerney, F.A., McElwain, J.C., 2019. Terrestrial and marginal-marine
656 records of the mid-Cretaceous Oceanic Anoxic Event 2 (OAE 2): High-resolution
657 framework, carbon isotopes, CO₂ and sea-level change. *Palaeogeog.*
658 *Palaeoclimatol. Palaeoecol.* 542, 118–136.

659 Lin, W., Bhattacharya, J.P., Jicha, B.R., Singer, B.S., Matthews, W., 2021. Has Earth
660 ever been ice-free? Implications for glacio-eustasy in the Cretaceous greenhouse
661 age using high-resolution sequence stratigraphy. *Geol. Soc. Am. Bull.* 133, 243–
662 252.

663 Miller, K.G., Wright, J.D., Browning, J.V., 2005. Visions of ice sheets in a greenhouse
664 world. *Mar. Geol.* 217, 215–231.

665 Nádaskay, R., Uličný, D., 2014. Genetic stratigraphy of Coniacian deltaic deposits of the
666 northwestern part of the Bohemian Cretaceous Basin. *Z. Dt. Ges. Geowiss.* 165,
667 547–575.

668 O'Brien, C.L. and 26 others, 2017. Cretaceous sea-surface temperature evolution:
669 Constraints from TEX₈₆ and planktonic foraminiferal oxygen isotopes. *Earth-Sci.*
670 *Rev.* 172, 224–247.

671 Olszewska-Nejbert, D., 2004. Development of the Turonian/Coniacian hardground
672 boundary in the Cracow Swell area (Wielkanoc quarry, southern Poland). *Geol.*
673 *Quart.* 48, 159–170.

674 Pattison, S.A.J., Walker, R.G., 1992 Deposition and interpretation of long, narrow
675 sandbodies underlain by a basinwide erosion surface: Cardium Formation,
676 Cretaceous Western Interior Seaway, Alberta, Canada. *J. Sedim. Petrol.* 62, 292–
677 309.

678 Plint, A.G., 1988. Sharp-based shoreface sequences and "offshore bars" in the Cardium
679 Formation: Their relationship to relative changes in sea level. In: Wilgus, C.K.,
680 Hastings, B.S., Posamentier, H.W., van Wagoner, Ross, C.A., Kendall, C.G. St.C.,
681 (Eds.), *Sea Level Changes: An Integrated Approach*. Soc. Econ. Paleontol. Miner.,
682 Spec. Pub. 42, 357–370.

683 Plint, A.G., Kreitner, M.A., 2007. Extensive, thin sequences spanning Cretaceous
684 foredeep suggest high-frequency eustatic control: Late Cenomanian, Western
685 Canada foreland basin. *Geology* 35, 735–738.

686 Plint, A.G., Walker, R.G., Bergman, K.M., 1986. Cardium Formation 6. Stratigraphic
687 framework of the Cardium in subsurface. *Bull. Can. Petrol. Geol.* 34, 213–225.

688 Plint, A.G., Krawetz, J.R., Buckley, R.A., Vannelli, K.M., Walaszczyk, I., 2018. Tectonic,
689 eustatic and climatic controls on marginal marine sedimentation across a flexural
690 depocentre: Paddy Member of Peace River Formation (Late Albian), Western
691 Canada Foreland Basin. *Deposit. Record* 4, 4–58.

692 Ray, D.C., van Buchem, F.S.P., Baines, G., Davies, A., Gréselle, B., Simmons, M.D.,
693 Robson, B., 2019. The magnitude and cause of short-term eustatic Cretaceous
694 sea-level change: A synthesis. *Earth-Sci. Rev.* 197, 102901
695 <https://doi.org/10.1016/j.earscirev.2019.102901>

696 Sames, B., Wagreich, M., Wendler, J.E., Haq, B.U., Conrad, C.P., Melinte-Dobrinescu,
697 M.C., Hu, X., Wendler, I., Wolfgring, E., Yilmaz, I.Ö., Zorina, S.O., 2016. Review:
698 Short-term sea-level changes in a greenhouse world - A view from the Cretaceous.
699 *Palaeogeog. Palaeoclimatol. Palaeoecol.* 441, 393–411.

700 Sames, B., Wagreich, M., Conrad, C.P., Iqbal, S., 2020. Aquifer-eustasy as the main
701 driver of short-term sea-level fluctuations during Cretaceous hothouse climate
702 phases. In: Wagreich, M., Hart, M.B., Sames, B., Yilmaz, I. (Eds.), *Cretaceous*
703 *climate events and short-term sea-level changes.* Geol. Soc. London, Spec. Pub.
704 498, 9–38 <https://doi.org/10.1144/SP498-2019-105>.

705 Shank, J.A., 2012. *Sedimentology and allostratigraphy of the Cardium Formation*
706 *(Turonian–Coniacian) in southern Alberta and equivalent strata in northern*
707 *Montana.* PhD thesis, Univ. Western Ontario, 374 p.

708 Shank, J.A., Plint, A.G., 2013. Allostratigraphy of the Upper Cretaceous Cardium
709 Formation in subsurface and outcrop in southern Alberta, and correlation to
710 equivalent strata in northwestern Montana, *Bull. Can. Petrol. Geol.* 61, 1–40.

711 Siegenthaler, U., Sarmiento, J.L., 1993. Atmospheric carbon dioxide and the ocean.
712 *Nature* 365, 119–125.

713 Simmons, M.D., Miller, K.G., Ray, D.C., Davies, A., van Buchem, F.S.P., Gréselle, B.,

714 2020. Phanerozoic eustasy. In: Gradstein, F.M., Ogg, J.M. Schmitz, M.D., Ogg,
715 G.M. (Eds.), A Geologic Time Scale, Chapter 13, Elsevier, Amsterdam, 357–400.

716 Uličný, D. Laurin, J., Čech, S., 2009. Controls on clastic sequence geometries in a
717 shallow-marine transtensional basin: the Bohemian Cretaceous Basin, Czech
718 Republic. *Sedimentology* 56, 1077–1114.

719 Uličný, D., Jarvis, I., Gröcke, D.R., Cech, S., Laurin, J., Olde, K., Trabucho-Alexandre,
720 J., Švábenická, L., Pedentchouk, N., 2014. A high-resolution carbon-isotope
721 record of the Turonian stage correlated to a siliciclastic basin fill: Implications for
722 mid-Cretaceous sea-level change. *Palaeogeog. Palaeoclimatol. Palaeoecol.* 405,
723 42–58.

724 Voigt, S., Gale, A.S., Voigt, T., 2006. Sea-level change, carbon cycling and
725 palaeoclimate during the Late Cenomanian of northwest Europe: an integrated
726 palaeoenvironmental analysis. *Cret. Res.* 27, 836–858.

727 Voigt, S., Wagerich, M., Surlyk, F., Walaszczyk, I., Uličný, D. Čech, S., Voigt, T.,
728 Wiese, F., Wilmsen, M., Niebuhr, B., Reich, M., Funk, H., Michalík, J., Jagt,
729 J.W.M., Felder, P.J., Schulp A.S., 2008. Cretaceous. In: *Geology of Central*
730 *Europe, Volume 2: Mesozoic and Cenozoic* (ed. by T. McCann), 923–997. The
731 Geological Society, London.

732 Wagerich, M., Lein, R., Sames, B., 2014. Eustasy, its controlling factors, and the limno-
733 eustatic hypothesis – concepts inspired by Eduard Suess. *Austrian J. Earth*
734 *Sci.* 107, 115–131.

735 Walaszczyk. I., Wood, C.J., Lees, J.A., Peryt, D., Voigt, S., Wiese, F., 2010. The
736 Salzgitter-Salder quarry (Lower Saxony, Germany) and Słupia Nadbrzeżna river
737 cliff section (central Poland): a proposed candidate composite Global Boundary
738 Stratotype Section and Point for the base of the Coniacian Stage (Upper
739 Cretaceous). *Acta Geol. Pol.* 60, 445–477.

740 Walaszczyk, I., Shank, J.A., Plint, A.G., Cobban, W.A., 2014. Inter-regional correlation
741 of disconformities in Upper Cretaceous strata, Western Interior Seaway:
742 Biostratigraphic and sequence-stratigraphic evidence for eustatic change. *Geol.*
743 *Soc. Am. Bull.* 126, 307–316.

744 Wendler, I., 2013. A critical evaluation of carbon isotope stratigraphy and
745 biostratigraphic implications for Late Cretaceous global correlation. *Earth-Sci. Rev.*
746 126, 116–146.

747 Wendler, J.E., Wendler, I., 2016. What drove sea-level fluctuations during the mid-
748 Cretaceous greenhouse climate? *Palaeogeog. Palaeoclimatol. Palaeoecol.* 441:
749 412–419.

750 Wendler, J.E., Wendler, I., Vogt, C., Kuss, J., 2016. Link between cyclic eustatic sea-
751 level change and continental weathering: Evidence for aquifer-eustasy in the
752 Cretaceous. *Palaeogeog. Palaeoclimatol. Palaeoecol.* 441, 430–437.

753 Wilmsen, M., 2007. Integrated stratigraphy of the upper Lower – lower Middle
754 Cenomanian of northern Germany and southern England. *Acta Geol. Pol.* 57,
755 263–279.

756

757 **Figure Captions**

758 **Fig. 1.** Turonian palaeogeographic map of the Earth (after R. Blakey,
759 cpgeosystems.com) showing the location of the two study areas.

760

761 **Fig. 2.** Bio-, chemo-, and chronostratigraphic framework of this study. Shown are the
762 Bohemian and WCFB carbon-isotope records (Bch-1 core, both $\delta^{13}\text{C}_{\text{carb}}$ and $\delta^{13}\text{C}_{\text{org}}$;
763 Horseshoe Dam, $\delta^{13}\text{C}_{\text{org}}$) along with the Chalk $\delta^{13}\text{C}_{\text{carb}}$ reference curve (Jarvis et al.,
764 2006) and the Colorado composite $\delta^{13}\text{C}_{\text{org}}$ record (Joo and Sageman, 2014). All data
765 plotted in the time domain using the age model of Laurin et al. (2015). Interpreted
766 positions of named carbon-isotope events and their abbreviations follow Uličný et al.
767 (2014) and Jarvis et al. (2015). Hiatuses in the Western Canadian succession follow
768 nomenclature of key surfaces in the WCFB explained in text. T4 –T6 and Co1 – labelled
769 CIEs in the Colorado composite curve from Joo and Sageman (2014). LO – lowest
770 occurrence of index macrofossil.

771

772 **Fig. 3.** Comparison of lithological, C-isotope records, and biostratigraphic tie points
773 between the sections in Alberta and Bohemia. The Si/Al ratio in the Bch-1 section has
774 been used as a supplementary criterion for interpreting the transgressive-regressive
775 history. In part of the Upper Turonian, the astrochronological interpretation of the Si/Al
776 data (after Laurin in Chroustová et al., 2021) helped to estimate the timescale of
777 lithological cyclicity in Bohemia, and of the E3 and E4 hiatuses in Alberta. "~100 kyr" =

778 inferred short-eccentricity signal (Gaussian filter, 0.035 ± 0.02 cycles/m); " ~ 20 kyr" =
779 inferred precessional signal (Gaussian filter, 0.21 ± 0.06 cycles/m; Chroustová et al.,
780 2021). Diagenetic silicification has altered the primary record in the topmost part of the
781 Si/Al record in Bch- 1.

782

783 **Fig. 4.** Summary dip section through the Cardium alloformation, modified after Shank
784 and Plint (2013). Allomembers are defined by regionally-mapped composite 'E/T'
785 (erosion/transgression) surfaces that record sea-level fall and subaerial or submarine
786 erosion, followed by transgressive erosion and reworking. E and T surfaces define the
787 lower and upper boundaries of conglomeratic lowstand shoreface deposits, but merge
788 into composite surfaces to landward and seaward. Note that surface 'E5.7' is present in
789 the Horseshoe Dam area but has not been mapped regionally, as have the other
790 surfaces. In the original scheme of Plint et al. (1986) the Kakawa 'allomember',
791 comprising a shoreface sandstone, was defined (erroneously) on partially
792 lithostratigraphic grounds, and hence letters (N), (B) and (H) are appended to denote
793 temporal equivalence of shoreface sandstone facies to time-equivalent offshore facies
794 of the Nosehill, Bickerdike and Hornbeck allomembers. Thin tongues of coastal plain
795 facies underlie the E5, E6 and E7 surfaces in the far western part of the basin. The
796 coastal plain facies of the Musreau allomember include muddy floodplain and lagoonal
797 mudstones, and small-scale channel-filling sandstone bodies, but no palaeovalleys are
798 known on any bounding surface.

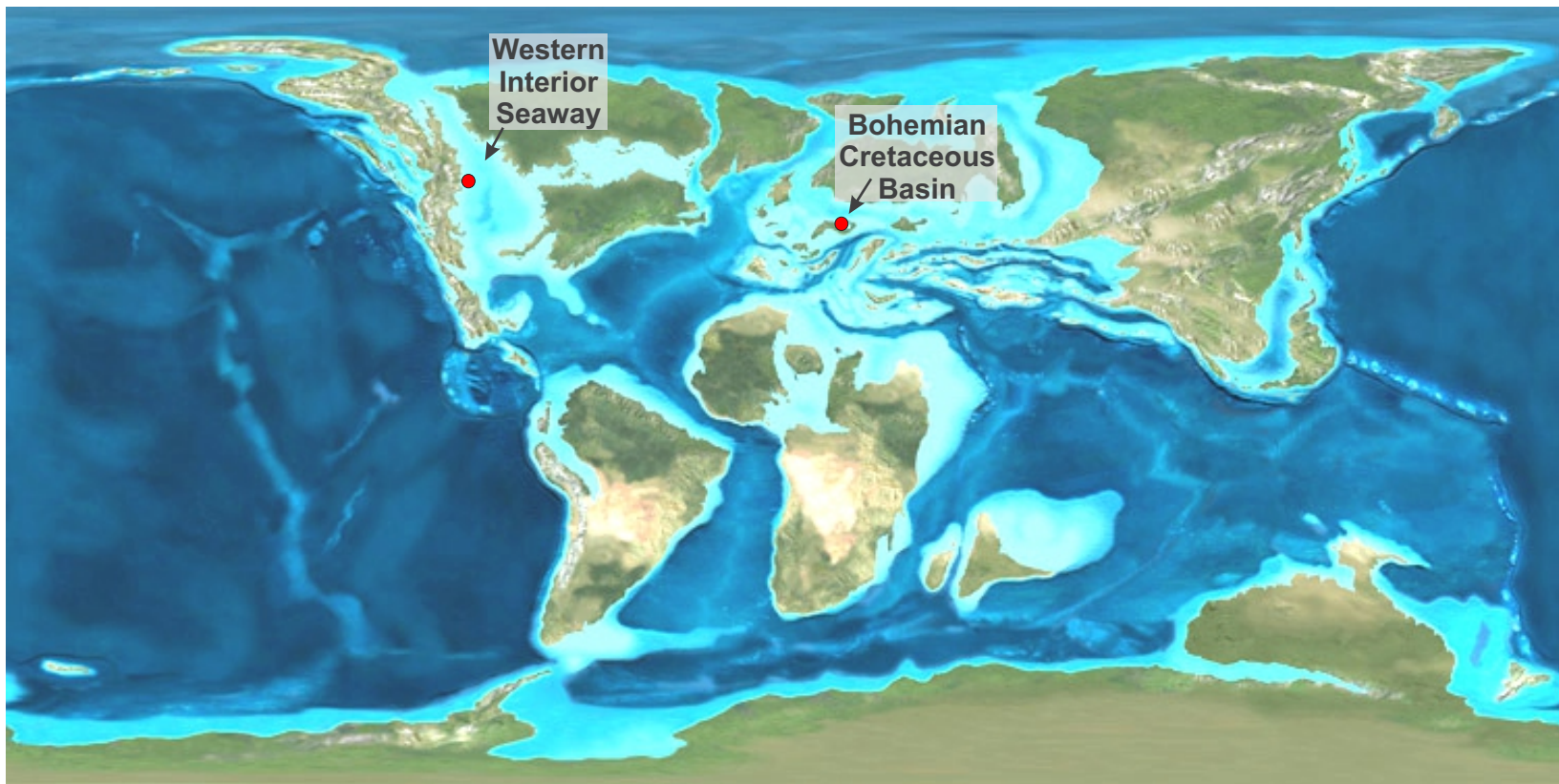
799

800 **Fig. 5.** Schematic, along-dip correlation panel of showing sedimentary units in NE
801 Bohemia, across the Turonian–Coniacian boundary (modified after Čech and Uličný,
802 2021). Horizontal scale is approximate due to projection of some sections into the
803 correlation line (see map in Fig. S.3), and to the SE of section 28, a great distance to
804 the Bch-1 reference core. Datum varies due to changes of depositional geometry in
805 time and space: to the NW of section 5, correlation is hung on top of sequence HS 2,
806 between sections 4 and 25 on top of sequences HS 7 and HS 6.

807

808 **Fig. 6.** Simplified chronostratigraphic (Wheeler) diagrams based on cross-sections of
809 the study interval in both WCFB and BCB, correlated using the Bch-1 $\delta^{13}\text{C}_{\text{org}}$ record and
810 biostratigraphic datums plotted in the time domain (based on age model of Laurin et al.,
811 2015). Abbreviations: *Ccc* - *Cremnoceramus crassus crassus*; *Cci* - *C. crassus*
812 *inconstans*; *Cde*, *C. def. erectus* - *C. deformis erectus*; *Cww* - *C. waltersdorfensis*
813 *waltersdorfensis*; *Cwh* - *C. waltersdorfensis hannovrensis*, *Mh* – *Mytiloides herbichi*.
814 Hyph. Ev. - Hyphantoceras Event assemblage. Filtered signal of 400 kyr-scale cyclicity
815 shown is derived from Si/Al data in Bch-1 (see Fig. 3, S4 and text for details). Derivation
816 of the eustatic curve and estimated magnitudes of eustatic change for selected cycles
817 are explained in text.

818



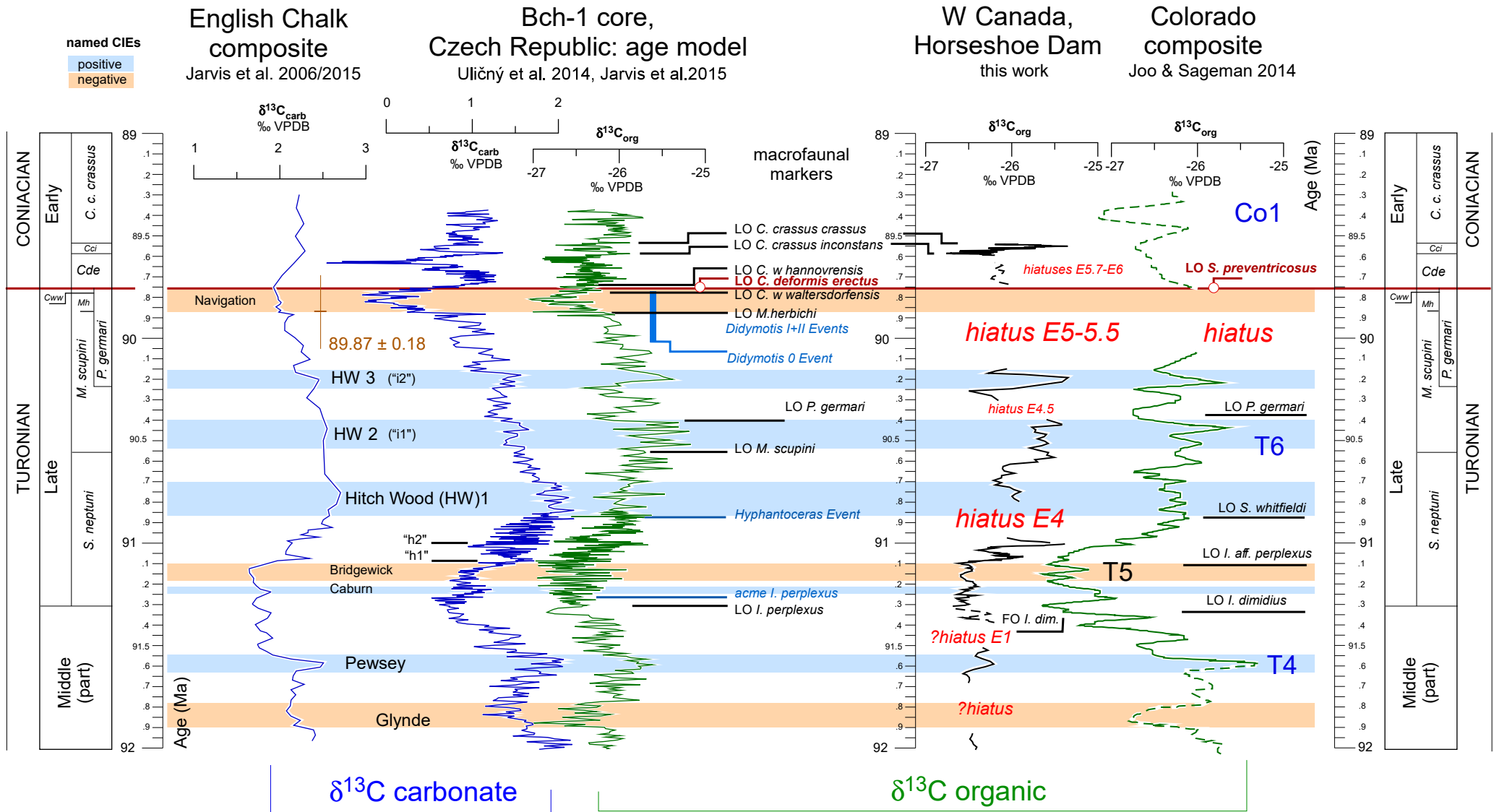
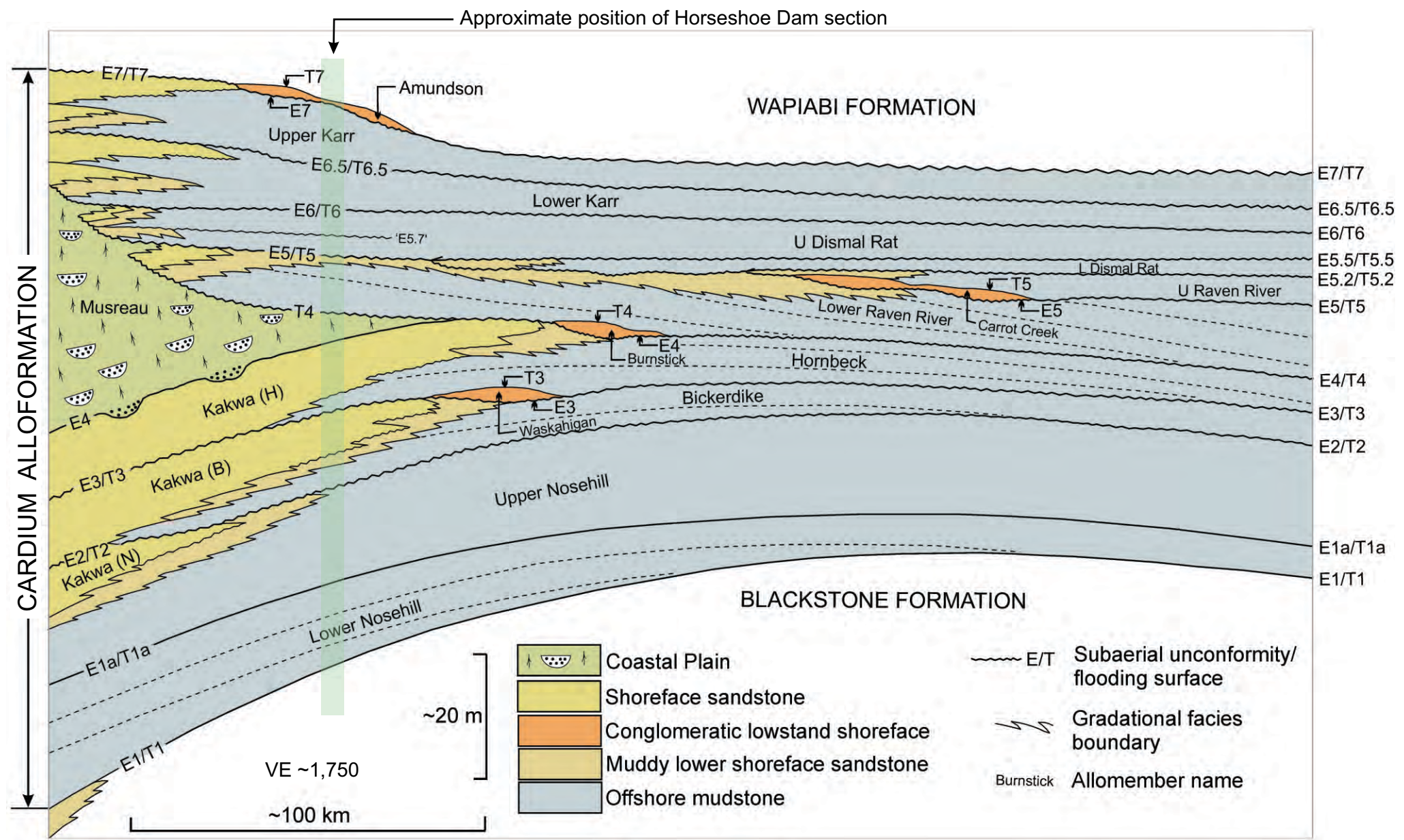
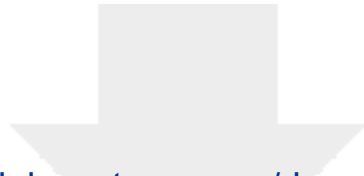


Figure 4

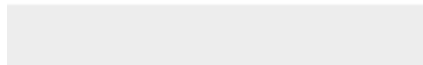




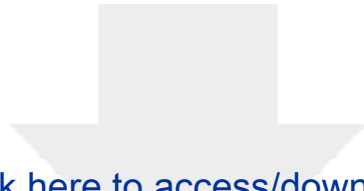
Click here to access/download

Figure (high-resolution)

Fig. 1 Turonian World map.jpg



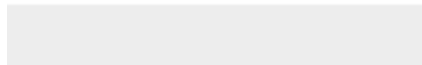




Click here to access/download

Figure (high-resolution)

Fig. 3 HSD-Bch correlation logs.jpg



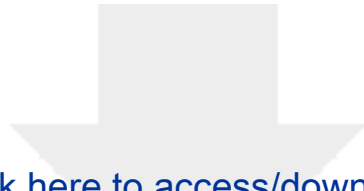


Click here to access/download

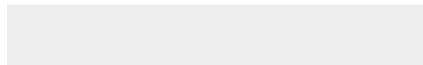
Figure (high-resolution)

Fig. 4 Cardium cross-section.jpg





Click here to access/download
Figure (high-resolution)
Fig. 5 Bohemia cross-section.jpg

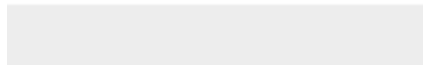




Click here to access/download

Figure (high-resolution)

Fig. 6 Chronostrat comparison.jpg





[Click here to access/download](#)

Supplementary material for online publication only
Alberta-Bohemia- Supplementary Material.pdf





Click here to access/download

Supplementary material for online publication only
Principal bounding surfaces - Supplementary Table
1.docx



[Click here to access/download](#)

Supplementary material for online publication only
Horseshoe Dam isotopic data.xls

